Mitochondria-Targeting Magnetic Composite Nanoparticles for Enhanced Phototherapy of Cancer

Ranran Guo, Haibao Peng, Ye Tian, Shun Shen, and Wuli Yang*

Photothermal therapy (PTT) and photodynamic therapy (PDT) are promising cancer treatment modalities in current days while the high laser power density demand and low tumor accumulation are key obstacles that have greatly restricted their development. Here, magnetic composite nanoparticles for dual-modal PTT and PDT which have realized enhanced cancer therapeutic effect by mitochondria-targeting are reported. Integrating PTT agent and photosensitizer together, the composite nanoparticles are able to generate heat and reactive oxygen species (ROS) simultaneously upon near infrared (NIR) laser irradiation. After surface modification of targeting ligands, the composite nanoparticles can be selectively delivered to the mitochondria, which amplify the cancer cell apoptosis induced by hyperthermia and the cytotoxic ROS. In this way, better photo therapeutic effects and much higher cytotoxicity are achieved by utilizing the composite nanoparticles than that treated with the same nanoparticles missing mitochondrial targeting unit at a low laser power density. Guided by NIR fluorescence imaging and magnetic resonance imaging, then these results are confirmed in a humanized orthotropic lung cancer model. The composite nanoparticles demonstrate high tumor accumulation and excellent tumor regression with minimal side effect upon NIR laser exposure. Therefore, the mitochondria-targeting composite nanoparticles are expected to be an effective phototherapeutic platform in oncotherapy.

1. Introduction

Cancer is one of the biggest threats to human's life and health.[1] In the face of such a challenge, tremendous efforts have been devoted to cancer therapy in the past century and some therapies have been applied in clinics, such as surgery, chemotherapy, and radiotherapy.[2] However, these conventional therapeutic approaches often suffer from harming normal cells and tissues, inducing drug resistance, damaging immune system, and increasing incidence of second cancers.[3] In recent years, phototherapy has attracted much attention for its minimally invasive selective feature in curing neoplastic diseases.[4] One major phototherapeutic approach is photothermal therapy (PTT), a treatment based on photo-absorbing materials and near infrared (NIR) laser to realize the transformation from optical energy into thermal energy, which can produce specific localized heat to kill cancer cells.[5] Nevertheless, the most usage of laser power density is relatively high, which is not applicable for clinical treatments as the power is higher than skin tolerance and the hyperthermia may also damage surrounding normal tissue.[6] Photodynamic therapy (PDT) is another promising modality, in which NIR light is utilized to trigger photosensitizer to generate reactive oxygen species (ROS) resulting in the apoptosis of cancer

R. Guo, H. Peng, Y. Tian, Prof. W. Yang
State Key Laboratory of Molecular Engineering
of Polymers
Department of Macromolecular Science
and Laboratory of Advanced Materials
Fudan University
Shanghai 200433, P. R. China
E-mail: wlyang@fudan.edu.cn

Dr. S. Shen
School of Pharmacy & Key Laboratory of Smart Drug Delivery
Fudan University
Shanghai 201203, P. R. China

cells and the elimination of the tumor.[7] Although PDT kills cancer cells in a fairly moderate manner,[8] low tumor accumulation of photosensitizer molecules hampers its usage in cancer therapy.[9] In this case, solutions to these problems in the PTT and PDT are required in order to broaden the clinical application range of phototherapy.

Mitochondria are vital cellular organelles to supply energy and are presumed the crucial regulators of cell death for its key role in apoptosis.[10] Hence, mitochondrial targeting has emerged as an attractive supplementary method to improve the therapeutic effect in cancer therapy.[11] Recently, Kim and co-workers successfully prepared iron oxide nanoparticles that could effectively target to mitochondria with better hyperthermia upon NIR laser irradiation.[12] Liu et al. developed mitochondrial targeted ruthenium complexes for two-photon PDT.[13] These works indicate that mitochondria-targeting is a powerful weapon in oncotherapy.

Herein, we report the preparation of mitochondria-targeting magnetic composite nanoparticles (MMCNs) for dual-modal PTT and PDT to realize enhanced cancer therapeutic effects. The composite nanoparticles with core-shell-shell architecture consist of spherical magnetite (Fe_3O_4) core, polydopamine (PDA) inner shell, and mesoporous silica ($mSiO_2$) outer shell. The Fe_3O_4[14] core and PDA[15] shell act as PTT agent and the $mSiO_2$ shell is utilized to load indocyanine green (ICG), a clinical photosensitizer approved by the US Food and Drug Administration (FDA), which can generate ROS upon NIR laser illuminance and partially convert light energy into heat energy to reinforce the PTT agent performance.[16] After surface modification of polyethylene glycol (PEG), transferrin (Tf),[17] and lipophilic triphenyphosphonium cation (TPP),[18] the composite nanoparticles can selectively target to the cancer cells and further be delivered to mitochondria. Upon NIR laser exposure, local hyperthermia and cytotoxic ROS are generated simultaneously to specifically induce mitochondria dysfunction, which amplifies the cancer cell apoptosis and thus reduces the demand of laser power to kill cancer cells. Furthermore, owing to the properties of Fe_3O_4 core and ICG, the MMCNs demonstrate NIR fluorescence imaging and magnetic resonance imaging (MRI) abilities. After in vivo administration, the composite nanoparticles are able to ablate tumor xenograft with NIR laser exposure at a relatively low power density and show no long-term systemic toxicity, exhibiting immense potential in cancer therapy.

2. Results and Discussion

2.1. Preparation of MMCNs

The preparation of MMCNs is illustrated in **Figure 1**a. First, the Fe_3O_4 cores are fabricated with a solvothermal method reported previously[19] with their transmission electron microscopy (TEM) image shown in Figure 1bi. Then PDA layer is coated on the surface of Fe_3O_4 cores by the self-polymerization of dopamine[20] and can be visualized clearly in the TEM image (Figure 1bii). Considering the influence of PDA layer thickness on the photothermal effect of the composite nanoparticles,[21] Fe_3O_4@PDA with a 20 nm thick

PDA layer is used (as measured in TEM images). After PDA coating, the hydrodynamic diameter of the particles increases from 176 to 208 nm as measured with dynamic light scattering (DLS, Table S1, Supporting Information). Thermogravimetric analysis (TGA, Figure S1, Supporting Information) also indicates the existence of PDA layer. The obtained Fe_3O_4@PDA is further used as a core and the mesoporous silica ($mSiO_2$) shell is prepared by a sol–gel process with tetraethoxysilane (TEOS) as silica source and cetyltrimethylammonium bromide (CTAB) as the pore template. For further surface modification, amine groups are used to functionalize the $mSiO_2$ outer shell before the removal of CTAB template. The mesoporous structure of the trilayer composite nanoparticles is confirmed by the N_2 sorption isotherms (Figure S2, Supporting Information), which reveal a typical type IV curve with a surface area of 451 m² g⁻¹ and a mean pore diameter of 2.7 nm. In addition, TGA results (Figure S1, Supporting Information) show the obtained Fe_3O_4@PDA@mSiO_2 has a weight loss of 10 wt%, lower than that of Fe_3O_4@PDA (24 wt%), which is attributed to the silica outer shell.

Then, N-hydroxysuccinimide ester (NHS)-terminated PEG is grafted on the surface of Fe_3O_4@PDA@mSiO_2 through the reaction between the NHS groups and amine groups, and the PEG-grafted Fe_3O_4@PDA@mSiO_2 is denoted as magnetic composite nanoparticle (MCN). TGA results show the MCNs have an additional weight loss of 15 wt% compared with Fe_3O_4@PDA@mSiO_2 (Figure S1, Supporting Information), which results from the decomposition of the modified PEG chains. Furthermore, Tf is thiolated and linked to the other end of the PEG chains as previously reported.[22] In the TGA curves (Figure S1, Supporting Information), Tf-linked MCNs (MCN-Tf) show an external weight loss of 8 wt%, which is ascribed to the linked Tf. Finally, the TPP groups are introduced on the surface of MCN-Tf by activated carboxy group-amine coupling reaction,[23] and MMCNs are obtained. The X-ray photoelectron spectroscopy spectrum of MMCNs reveals an increase in phosphorus atoms, thereby confirming the successful surface modification of TPP (Figure S3, Supporting Information). The TEM image of the resultant MMCNs is displayed in Figure 1biii, which clearly shows the mesoporous shell and the DLS measurement of MMCNs in phosphate buffered saline (PBS) indicates a hydrodynamic diameter of 275 nm with narrow distribution (Table S1, Supporting Information). The MMCNs also show an excellent dispersity in biological media such as serum free media and serum-containing media (Table S2, Supporting Information), ensuring their stability in the physiological aqueous condition.[24]

2.2. The Photothermal Effect of ICG-Loaded MMCNs

ICG is subsequently loaded into the mesopores of the MMCNs with a loading content of 8.0%. Its release behavior indicates that ICG is quite stable in the mesopores with only 16% release in 24 h (Figure S4, Supporting Information), which may be attributed to its zwitterionic amphiphilic nature.[25]

The UV–vis–NIR spectra (Figure 1c) show that owing to the absorption contribution of ICG, the PBS dispersion
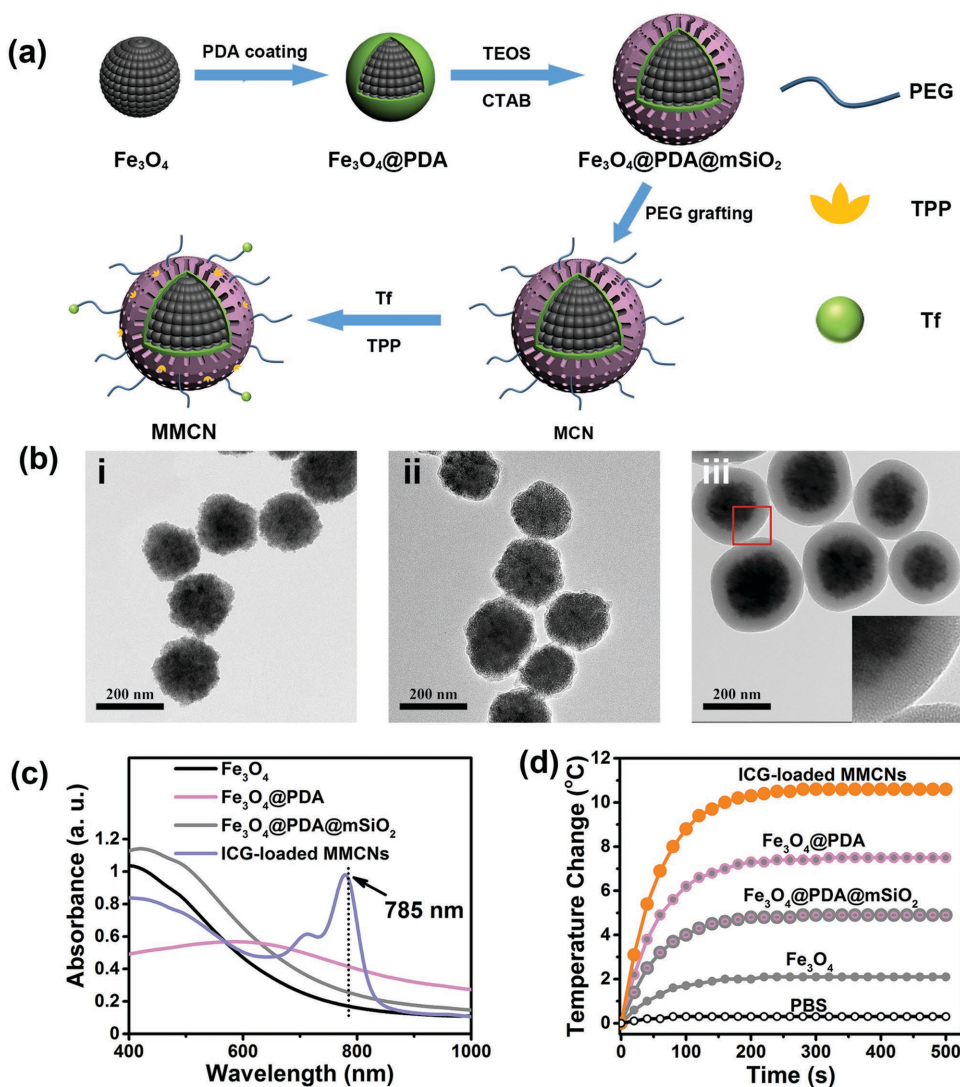
Figure 1. a) Schematic illustration of the preparation procedure of mitochondria-targeting magnetic composite nanoparticles (MMCNs). The diagram is not drawn to scale. b) TEM images of (i) Fe_3O_4, (ii) Fe_3O_4@PDA, and (iii) MMCNs. Insert: enlarged image of marked area. c) UV–vis–NIR absorption spectra of the aqueous nanoparticle dispersion at an equivalent concentration of 50 µg mL^{-1}. d) The photothermal response of the aqueous nanoparticle dispersion (50 µg mL^{-1}) with a NIR laser (785 nm, 0.5 W cm^{-2}). PBS is used as a negative control.

of ICG-loaded MMCNs exhibited three times higher NIR absorption than Fe_3O_4@PDA@mSiO$_2$ at 785 nm (at an equivalent concentration of 50 µg mL^{-1}). To further confirm the photothermal effect, different samples at the same concentration of 50 µg mL^{-1} are exposed to the 785 nm NIR laser with a power density of 0.5 W cm^{-2} for 500 s. As depicted in Figure 1d (Figure S5, Supporting Information), ICG-loaded MMCNs show a photothermal performance with temperature elevated ≈10 °C, better than Fe_3O_4@PDA (≈7 °C), resulting from the additional photothermal contribution of ICG.[16e]

2.3. Endocytosis and Colocalization of MMCNs

As shown in **Figure 2**a, MMCNs, with targeting ligand on the surface, are expected to enter into cancer cells through Tf receptor-mediated endocytosis,[17] endosome escape,[26]

and further target to mitochondria due to the electrostatic interaction between the mitochondria membrane and the lipophilic TPP cations.[10a]

To evaluate the uptake efficiency of MMCNs by cancer cells in vitro, human adenocarcinomic alveolar basal epithelial cell line (A549 cells) is used as model. A549 cells are incubatd with ICG-loaded composite nanoparticles for 4 h and the cells with nanoparticles internalized can be detected for the fluorescence from ICG molecules using a flow cytometry. Figure 2b shows the uptake efficiencies of MMCNs and MCN-Tf which are almost twice that of Tf-missing MCNs, indicating that Tf is a key factor in the internalization of the composite nanoparticles and TPP has little effect on the endocytosis. As a comparison study, there is no obvious uptake difference between MMCNs and MCNs in 293T cells (normal cells) (Figure S6, Supporting Information), which further demonstrates the selective targeting effect of MMCNs induced by Tf.
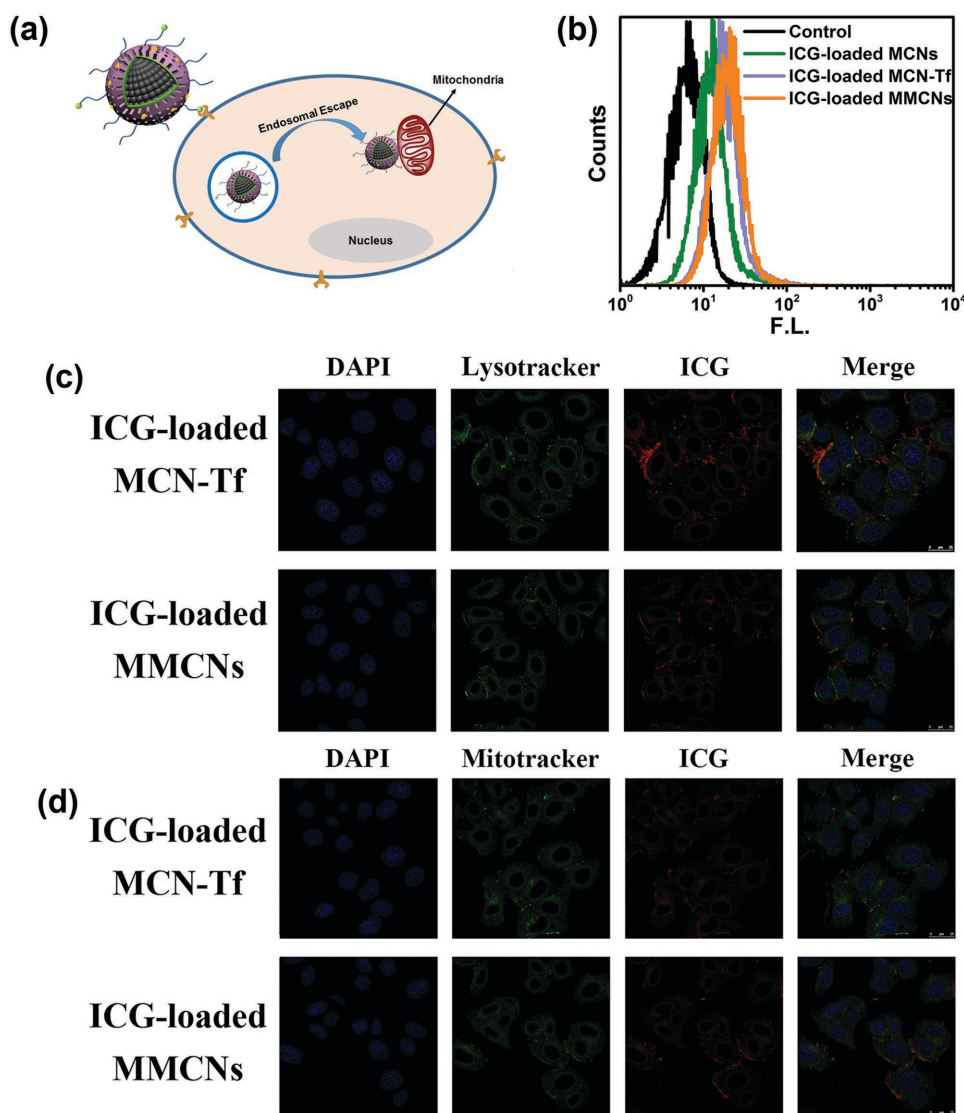
Figure 2. a) Schematic diagram of endocytosis and mitochondria-targeting of MMCNs. b) Flow cytometry analysis to visualize the endocytosis of the nanoparticles. c) CLSM images of A549 cells incubated with MCN-Tf or MMCNs. The nucleus and lysosomes of A549 cells are stained with DAPI (blue) and Lysotracker (green), respectively. d) CLSM images of A549 cells incubated with MCN-Tf or MMCNs. The nucleus and mitochondria of A549 cells are stained with DAPI (blue) and Mitotracker (green), respectively.

The use of nanoparticles in organelle-targeting is often limited by the fact that the nanoparticles are taken up by the endosomal pathway, where endosomes serve as a barrier to organelle trafficking.[26] It is reported that the high net positive charge from lipophilic cationic groups such as TPP cation has the potential to promote endosomal escape through a proton-sponge effect.[27] To verify that our MMCNs have endosome escapability and are not engaged in trafficking to lysosomes, we studied a colocalization of MMCNs with lysosomes. 4,6-diamidino-2-phenylindole (DAPI) and Lysotracker are utilized to treat cells that have been cultured with MMCNs and MCN-Tf for 4 h, respectively. Then the samples are subjected to confocal laser scanning microscopy (CLSM). The confocal fluorescence microscopic images are shown in Figure 2c, in which the blue fluorescence from DAPI represents nucleus, the green one from Lysotracker represents lysosomes and the red one from ICG represents

the nanoparticles. The MCN-Tf is distributed in both lysosomes and the cytoplasm, whereas MMCNs exhibit lysosomal escape ability.

To identify the mitochondria-targeting effect of MMCNs, DAPI and Mitotracker are utilized to treat cells that have been cultured with MMCNs and MCN-Tf for 4 h, respectively. The confocal fluorescence microscopic images are shown in Figure 2d, in which the green fluorescence from Mitotracker represents mitochondria. From the view of merged picture, the fluorescence of mitochondria overlaps with that of MMCNs while partial overlap is observed in the MCN-Tf treated cell, suggesting the localization of MMCNs to the mitochondria. Using another high-quantum-yield NIR dye, Cy7, as the cargo to track the nanoparticles, the CLSM images with a higher NIR fluorescence intensity are obtained (Figure S7, Supporting Information), which also proves the mitochondria-targeting effect of MMCNs.

The mitochondria-targeting effect of MMCNs is additionally corroborated by inductively coupled plasma atomic emission spectrometer (ICP-AES), since the presence of Fe elements in MMCNs allows sensitive quantification of the metal content in the cellular compartments after subtracting the baseline Fe levels in different organelles of untreated cells.[28] Remarkably, the Fe quantification evidences a significant accumulation of MMCNs in the mitochondria (Table S3, Supporting Information). And the TPP groups change the cellular distribution of the composite nanoparticles, since under a same incubation condition, the accumulation of MCN-Tf in mitochondria is excluded, which is in good agreement with the microscopic colocalization studies.

2.4. ROS Generation of ICG-Loaded MMCNs

To detect the ROS generation of ICG-loaded MMCNs upon NIR laser irradiation, the probe 1,3-diphenylisobenzofuran (DPBF) is used, as ROS can oxidize DPBF and quench its fluorescence.[29] Free ICG, MMCNs, and ICG-loaded MMCNs dispersions are mixed with DPBF and the fluorescence of DPBF is measured after 785 nm laser irradiation (5 min, 0.5 W cm^{-2}). As depicted in **Figure 3**a, the fluorescence intensities of free ICG and ICG-loaded MMCNs sample both have a rapid decline, indicating the capability of ICG-loaded MMCNs to produce ROS continuously. Whereas, comparing to free ICG, ICG-loaded MMCNs have a low decline rate of fluorescence intensity, resulting from the escape time of ROS from the mesopores of MMCNs.

We also investigate the intracellular ROS production of ICG-loaded MMCNs. Another ROS probe dichlorofluorescein diacetate (DCFDA) is used, which can be oxidized by ROS into dichlorofluorescein (DCF) with bright green fluorescence.[30] A549 cells are incubated with ICG-loaded MMCNs for 4 h, then DCFDA is added before subjected to flow cytometer. As shown in Figure 3b, obvious fluorescence of DCF can be detected after a 785 nm laser irradiation but none without laser. Besides, when we add an ROS inhibitor N-acetylcysteine (NAC),[29b] the fluorescence signal declined significantly. In order to observe the intracellular ROS generation more intuitive, the samples above are also measured with CLSM. In Figure 3c, the control group and ICG-loaded MMCNs group both show no fluorescence suggesting no ROS is produced, while the cells internalized with ICG-loaded MMCNs emit bright green fluorescence when treated with laser, suggesting ICG-loaded MMCNs can generate ROS in live cells under NIR laser irradiation.

2.5. In Vitro Phototherapy

In order to confirm the therapeutic effect, the A549 cells are cultured with ICG-loaded MMCNs and treated with 785 nm NIR laser irradiation (5 min, 0.5 W cm^{-2}). The treated cells are first costained with Annexin-V-Fluorescein isothiocyanate (FITC) and propidium iodide (PI) and then subjected to flow cytometer. As shown in **Figure 4**a, the phototherapy utilizing ICG-loaded MMCNs is able to induce the apoptosis process among cancer cells and readily causes cell death, indicating the success of the mitochondria-induced
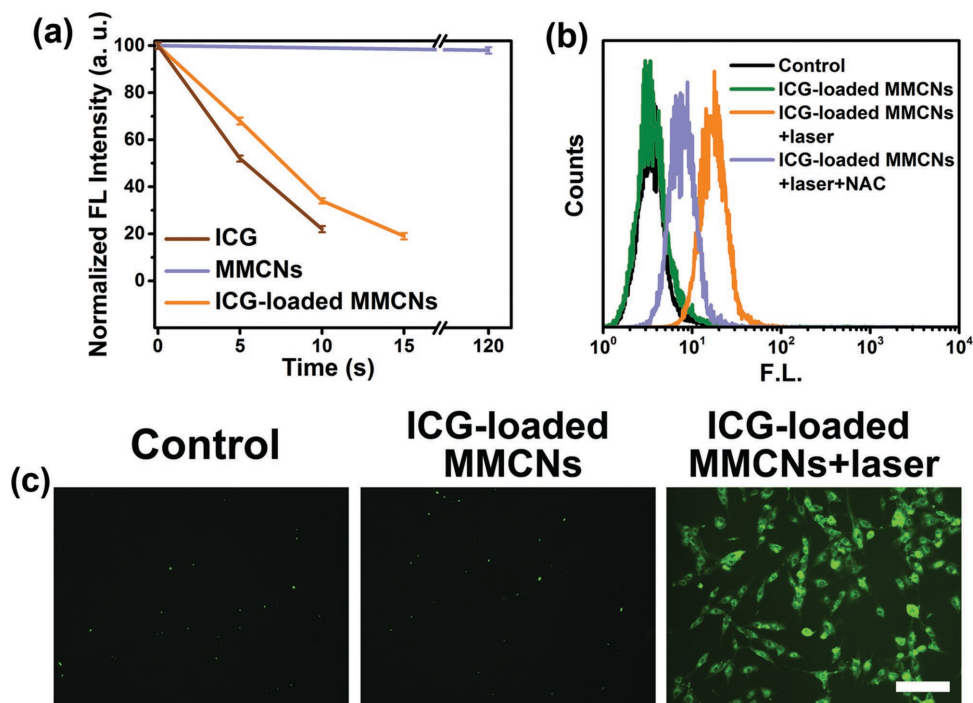

Figure 3. The generation of ROS. a) A comparison of the ability to generate ROS in different reaction systems containing DPBF under NIR irradiation by determining the related maximum of fluorescence intensity. The data are shown as mean value and standard derivation ($n = 3$). b) Intracellular ROS generation detected by the fluorescence of DCF with flow cytometry. c) CLSM images to visualize the intracellular ROS generation. White bar indicates 100 μm.
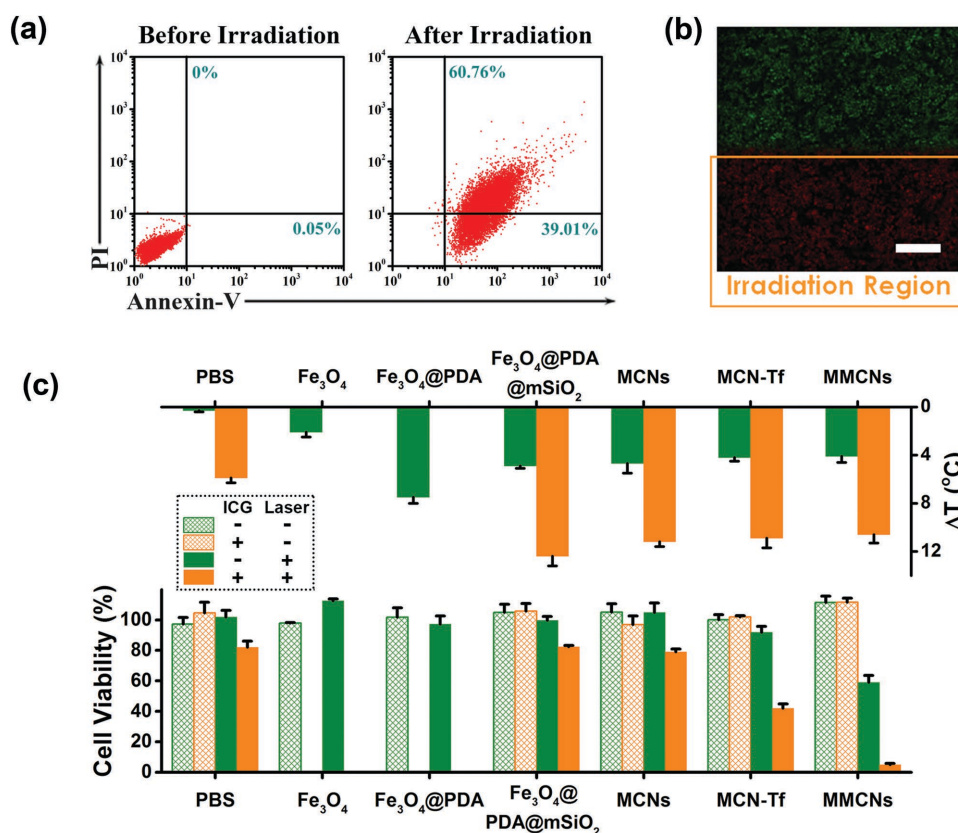
Figure 4. a) Flow cytometry analysis of A549 cells treated with ICG-loaded-MMCNs at the concentration of 50 µg mL^{-1} before (left) and after NIR laser irradiation (785 nm, 0.5 W cm^{-2}) for 300 s (right). The treated cells are double stained with Annexin-V-FITC and PI. b) Confocal images of calcein-AM (green, live cells) and PI (red, dead cells) costained A549 cells after laser irradiation for 300s. White bar indicates 1 mm. c) Growth inhibition results for treated cells and the temperature change in the laser illumination.

photography. Then the treated cells are costained with calcein acetoxymethyl ester (calcein-AM) and PI. In the CLSM picture (Figure 4b), we can clearly see that the cells in irradiation region are hardly alive which demonstrates the ICG-loaded MMCNs could specific kill cancer cells under local NIR laser irradiation.

To further identify the therapeutic effect of each component in ICG-loaded MMCNs, the MTT (MTT is (3-(4,5-dimethylthiazol-2-yl)-2,5-diphenyltetrazolium bromide) assay is carried out to detect the relative viabilities of A549 cells. As shown in Figure 4c, the groups without Tf or TPP (PBS, Fe$_3$O$_4$, Fe$_3$O$_4$@PDA, Fe$_3$O$_4$@PDA@mSiO$_2$, MCNs) exhibit high cell viability even with the laser irradiation, which is attributed to the low temperature rise and inefficient nanoparticles uptake. However, in MCN-Tf and MMCNs groups, the cell viability has a sharp decline when treated with laser, and compared to ICG-loaded MCN-Tf, ICG-loaded MMCNs group has obvious lower cell viability with almost one-tenth of that in ICG-loaded MCN-Tf group. These results suggest that Tf groups improve the uptake efficiency of the nanoparticles and the additional TPP groups could target mitochondria effectively. Moreover, these groups show nontoxic to cells without laser. Overall, the ICG-loaded MMCNs can induce large amounts of cell death with 785 nm laser irradiation at a relatively low power density (0.5 W cm^{-2}) as the mitochondria-targeting greatly increases the therapeutic effect of phototherapy.

2.6. Tumor Targeting and Imaging

The effect of cancer treatment depends largely on the amount of therapeutic agent accumulated in tumor site. We have verified the Tf groups on surface of MMCNs which induce higher uptake efficiency in A549 cells in vitro. In order to further investigate the enrichment performance of MMCNs at the tumor tissue and the distribution in vivo, we use A549 tumor-bearing BALB/c nude mice as animal model. ICG-loaded MMCNs are administered to two mice by intravenous injection at a dosage of 5 mg kg^{-1} and another two mice are given ICG-loaded MCNs as the control group. Then the mice were anesthetized at different time intervals and subjected to an optical small animal imaging system, where NIR fluorescence images are captured. As shown in **Figure 5**a, the images of mice treated with MMCNs exhibit rather stronger fluorescence signal at tumor site than the MCN-treated mice, and the time-dependent mean fluorescence signal intensity curves are recorded (Figure S8, Supporting Information), suggesting the excellent accumulation ability of MMCNs in tumor region under the effect of Tf groups. With the purpose to test in vivo distribution, mice are euthanized at two time points (6 and 24 h) and major organs (heart, liver, spleen, lung, kidneys, and tumor) are removed. As demonstrated in Figure 5b, in MCNs group, the image shows strong fluorescence signal from liver at 6 h and much weaker signal from tumor which implies the majority of MCNs are accumulated in liver. However, at the
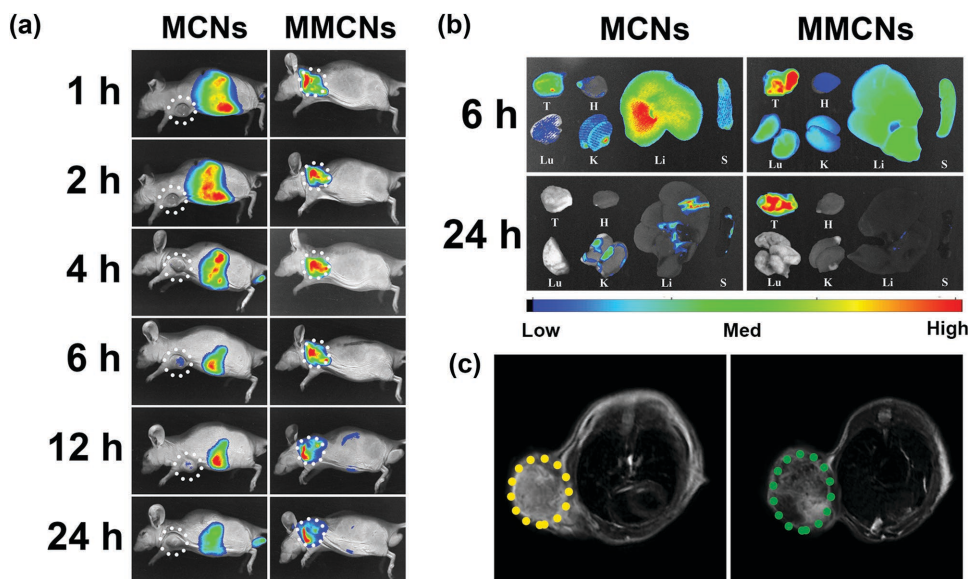
Figure 5. a) In vivo NIR fluorescence imaging of mice bearing A549 tumors after administration (tumor pointed out with white circle). b) Ex vivo imaging of tumor tissues and major organs at 6 or 24 h postinjection. T: tumor, H: heart, Li: liver, S: spleen, Lu: lung, K: kidney. c) In vivo T_2-MRI of mice after intravenous injection of MCNs (left, tumor pointed out with yellow circle) and MMCNs (right, tumor pointed out with green circle).

same time, MMCNs are mostly accumulated in tumor and a small amount in other organs. When the time prolongs to 24 h, the tumor of MMCNs group still exhibits obvious fluorescence signal while only negligible fluorescence signal can be observed in other tissues (Figure S9, Supporting Information). These results demonstrate the MMCNs possess eminent tumor targeting ability in vivo and can specifically persist in tumor during extended period of time.

The Fe_3O_4 core, the innermost component of MMCNs, has been applied broadly in MRI.[31] We examine its potential as contrast agents in MRI using a clinical MRI instrument. Figure S10a (Supporting Information) shows the transverse (T_2) phantom images of MMCNs at different concentration in aqueous medium. It reveals that the T_2 signal of MMCN has a significantly decrease following the concentration of MMCN increase and a r_2 value of 187 mm^{-1} s^{-1} is obtained (Figure S10b, Supporting Information). These results indicate the MMCNs are able to act as MRI contrast agent. When we measure the T_2 signal at the tumor site of treated mice at 6 h postinjection (Figure 5c; Figure S11, Supporting Information), the mouse injected with MMCNs shows a darkened image in tumor region which further confirm the targeting ability of MMCNs. The results demonstrate that the ICG-MMCNs possess excellent ability of fluorescence imaging and MRI imaging and could target tumor effectively.

2.7. In Vivo Phototherapy

On the basis of above results and analysis, we conduct the oncotherapy experiments in vivo. As illustrated in **Figure 6**a, A549 tumor-bearing BALB/c nude mice are divided into six groups of six mice per group, and then different samples are injected by tail intravenous injection with a dosage of 5 mg kg^{-1}: (1) PBS; (2) ICG molecules; (3) ICG-loaded MMCNs; (4) MMCNs; (5) ICG-loaded MCN-Tf;

(6) ICG-loaded MCN-TPP. According to the inference of fluorescence imaging (Figure 5a), we suppose the maximum accumulation of ICG-loaded MMCNs in the tumor region places between 4 and 6 h postinjection. However, it is necessary to leave enough time for the nanoparticles to target to mitochondria. As a result, we choose 6 h as the time point to implement NIR laser irradiation (785 nm, 0.5 W cm^{-2}, 300 s) for a better therapeutic effect. During NIR illumination, a thermal infrared camera is used to record the temperature of tumor site. As shown in Figure 6b and Figure S12 (Supporting Information), MMCN-treatment induces a 2.9 °C elevation of the mean temperature in the tumor region and the highest temperature of the tumor in the ICG-loaded MMCN-treated group is around 38 °C which is slightly higher than normal temperature of body, indicating that the tissue around tumor will not be injured by hyperthermia. Meanwhile, after laser irradiation, tumors are removed immediately from one mouse of each group for tissue section and image analysis. Although the temperature of tumor is far lower than which needed for killing cancer cells,[32] cells treated with ICG-loaded MMCNs are almost dead (Figure S13, Supporting Information) which is attributed to the effective targeting to mitochondria and NIR-triggered ROS generation.

To further evaluate the anticancer efficacy of ICG-loaded MMCNs, tumor growth rates (Figure S14, Supporting Information) are recorded and the final tumor weights (Figure 6c) are measured. The results show the tumors in group 1 (injected with PBS), group 2 (injected with ICG), and group 6 (injected with ICG-loaded MCN-TPP) grow rapidly, resulting from the inefficient enrichment of nanoparticles in tumor region. Group 4 and group 5 exert significantly slow growth rate, suggesting the therapeutic effect of mitochondria-targeting PTT and intracellular phototherapy, respectively. However, in group 3, though with the same relatively low laser power density, the tumors are completely eliminated, indicating that successful mitochondria-targeting greatly
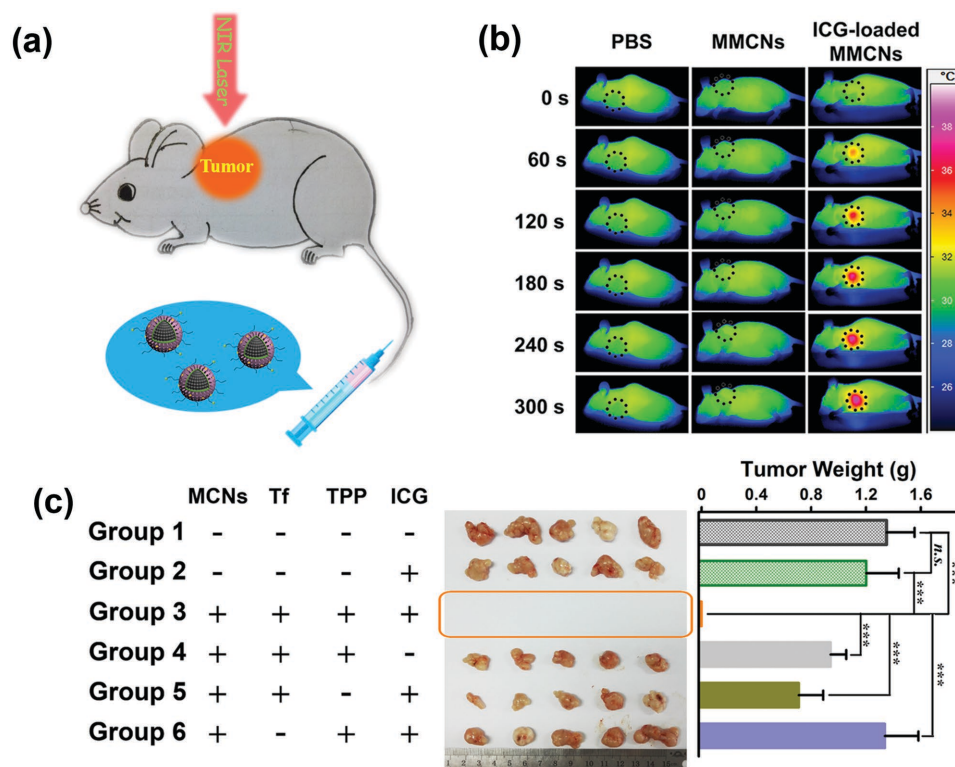
Figure 6. In vivo phototherapy. a) Schematic illustration of the therapeutic process of A549 tumors with the assistance of NIR laser. b) Thermal images of A549 tumor-bearing mice exposed to 785 nm laser for 5 min after the injection of PBS, MMCNs, and ICG-loaded MMCNs. c) Photograph (middle) and weights (right) of tumors after excision from each group. n.s. means no significant difference, and ***, $p < 0.001$.

reinforce the efficiency of PDT and PTT. These results imply ICG-loaded MMCNs own excellent therapeutic effect in the phototherapy of cancer.

2.8. In Vivo Toxicity

To confirm the safety of phototherapy utilizing ICG-loaded MMCNs, we investigate the biodistribution of ICG-loaded MMCNs in the major organs and tumor tissues after the therapy, which is quantified by ICP-AES according to the Fe content. As shown in **Figure 7**a, the remaining Fe elements are taken up predominantly in liver and spleen within two days,[33] and at the 14th d posttreatment, the Fe content is rather low in all tissues, suggesting the nanoparticles are almost excreted from these organs and cleared completely. In Figure 7b, the body weights of mice are recorded every other day after the treatment and there is no apparent weight loss in the group with ICG-loaded MMCNs injection, suggesting the nanoparticles do not induce severe systemic toxicity.[34] And at the 14th d postinjection, all mice have to be sacrificed because of the extensive tumor burden, and the major viscera (heart, liver, spleen, lung, and kidneys) are excised and costained by hematoxylin and eosin (H&E). In Figure 7c, compared to the control group, the mice injected with ICG-loaded MMCNs exhibit no obvious organ damage and inflammatory lesion. These data indicate that the ICG-loaded MMCNs with relatively low systemic toxicity are a promising phototherapy agent in oncotherapy.

3. Conclusion

In summary, we have prepared a novel multifunctional cancer therapy platform, ICG-loaded MMCNs, which successfully realizes the phototherapy upon NIR laser irradiation and greatly enhances the therapeutic effect by mitochondria-targeting. Moreover, the ICG-loaded MMCNs exhibit favorable potential as probes in NIR fluorescence imaging and MRI due to the properties of Fe_3O_4 component and ICG molecules. In vivo experiments confirm the multimode imaging functions and remarkable tumor inhibition effect of ICG-loaded MMCNs with almost nontoxicity at a low laser power density. Therefore, NIR light induced, multiple functions integrated ICG-loaded MMCNs are expected to have wide applications in the phototherapy of cancer.

4. Experimental Section

Synthesis of Fe_3O_4: Fe_3O_4 were synthesized using a solvent thermal method.[19] $FeCl_3 \cdot 6H_2O$ (0.54 g), trisodium citrate (0.24 g), and anhydrous sodium acetate (1.2 g) were dissolved in ethylene glycol (20 mL). After magnetic stirring for 30 min, the final suspension was transferred to a teflon-lined stainless-steel autoclave (50 mL), which was heated at 200 °C for 10 h. The obtained products were washed with ethanol and water three times with the assistance of a magnet and denoted as Fe_3O_4.

Synthesis of Fe_3O_4@PDA: The Fe_3O_4@PDA composite nanoparticles were synthesized by a solution oxidation method.[20] The
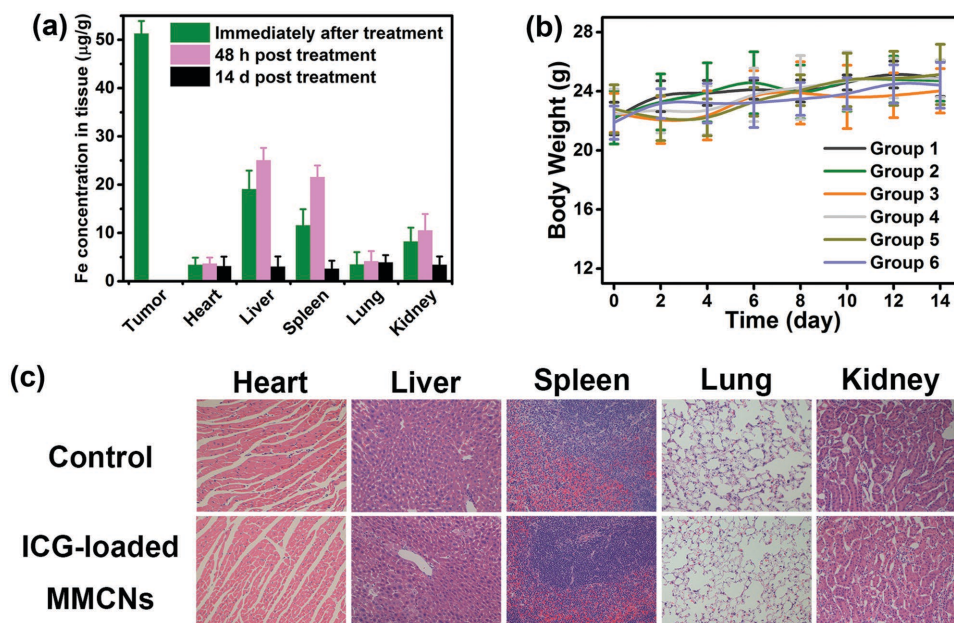
Figure 7. a) The biodistribution of the ICG-loaded MMCNs immediately, 48 h and 14 d after the treatment, based on ICP-AES analysis. b) Body weight change of the mice. c) H&E stained images of major organs collected from the mice (40×).

as-prepared Fe_3O_4 (25 mg) were dispersed in tris-Cl buffer solution (10×10^{-3} M, pH 8.5, 500 mL). Then dopamine hydrochloride (125 mg) was added into the above mixture. The resulting dispersion was continuously stirred for 1 h at room temperature. After the reaction, the nanoparticles were collected magnetically and washed with deionized water several times. The final products were dispersed in deionized water to obtain the desired Fe_3O_4@PDA composite nanoparticles.

Synthesis of Fe_3O_4@PDA@mSiO_2$: A mesoporous silica shell was coated on the surface of Fe_3O_4@PDA through dispersing Fe_3O_4@PDA (20 mg) into a mixture consisting of CTAB (0.3 g), deionized water (60 mL), and ethanol (20 mL). After stirred quickly for 30 min at 40 °C, aqueous ammonia solution (0.85 mL) and TEOS (0.15 mL) were added into the dispersion. The reaction was carried out for 24 h and Fe_3O_4@PDA@mSiO_2$ with CTAB was prepared. Then, to modify the -NH_2 groups on the surface of the nanocomposites, 3-aminopropyltriethoxysilane (100 μL) was added into the ethanol dispersion (50 mL) containing the prepared Fe_3O_4@PDA@mSiO_2$ with CTAB. The reaction was carried out for 6 h at 80 °C. Then CTAB was removed through dispersing Fe_3O_4@PDA@mSiO_2$ with CTAB in the ethanol solution of NH_4NO_3 (10 mg mL^{-1}), and the mixture was refluxed at 80 °C for 6 h and Fe_3O_4@PDA@mSiO_2$ was prepared.

Synthesis of MCNs: The obtained Fe_3O_4@PDA@mSiO_2$ (20 mg), maleimide poly(ethylene glycol) N-hydroxysuccinimide ester (Mal-PEG-NHS, M_w 2 kDa, 4 mg) and poly(ethylene glycol) N-hydroxysuccinimide ester (PEG-NHS, M_w 2 kDa, 16 mg) were dispersed in N,N-dimethylformamide (DMF, 20 mL). After stirred for 24 h, MCNs were fabricated.

Thiolation of Tf: Tf was modified with sulfydryl groups to obtain Tf-SH. A solution containing 2-[4-(2-hydroxyethyl)-1-piperazinyl] ethanesulfonic acid (HEPES, 30×10^{-3} M) and ethylene diamine tetraacetic acid (1×10^{-3} M) with a pH value of 8.5 was prepared, denoted as HEB. Tf (10 mg) was added in HEB solution (1 mL), and this solution was stirred for 20 min under dynamic nitrogen atmosphere. Then, a HEB solution of 2-iminothiolane hydrochloride (6.5×10^{-3} M, 0.1 mL) was added to the solution. After stirred at room temperature for 3 h, Tf-SH was prepared.

Synthesis of MCN-Tf: The obtained Tf-SH was added in a HEPES solution (20 mL, pH 7.4) containing the synthesized MCN. The reaction was carried out for 24 h, and MCN-Tf was prepared.

Synthesis of (3-Carboxyethyl) Triphenyl Phosphonium Bromide (CTPB)[35]: Triphenylphosphine (1.7 g) was added to a solution of 3-bromopropionic acid (1 g) in acetonitrile (2.5 mL). The resulting mixture was stirred at 80 °C for 24 h and then concentrated in vacuo. The residue was taken up with a minimal amount of chloroform and the product was precipitated from ethyl acetate. The white precipitate was filtered and washed three times with ethyl acetate, then dried at 40 °C under vacuum for 24 h to give the compound as a colorless solid with a yield of 78%. ^{1}H NMR (400 MHz, CDCl_3$, Figure S15, Supporting Information): $\delta = 10.34$ (br s, 1 H), 7.79–7.60 (m, 15 H), 3.72 (dt, 2 H), and 2.93 (dt, 2 H).

Activation of CTPB: CTPB was activated by N,N'-disuccinimidyl carbonate (DSC). DSC (32.8 mg), dissolved in 500 μL of chloroform was added into the solution of CTPB (50 mg) in chloroform at 0 °C. The reaction mixture was stirred at room temperature overnight. The chloroform was evaporated, and the system was freeze dried. The reaction mixture was dissolved in DMF at a concentration of 50 mg mL^{-1}, stored at −20 °C and used in the next reaction without additional purification.

Synthesis of MMCNs: MCN-Tf (20 mg) was dispersed in PBS (pH 8) and NHS-activated CTPB (2 mg) solution in DMF was added. The reaction mixture was stirred at room temperature for 4 h, washed with water and redispersed in water, and then MMCNs were fabricated.

ICG Loading and Release: ICG was dissolved in PBS (pH 7.4) with a concentration of 1 mg mL^{-1}. To encapsulate ICG into the nanoparticles, 10 mg of MMCNs were dispersed in 1.5 mL ICG solution, and stirred at room temperature for 12 h. Then, the nanoparticles were collected and washed with deionized water twice. The content of ICG encapsulated in nanoparticles was determined by optical absorption spectroscopy at 780 nm, the loading content is 8.0%. The loading of Cy7 dye was carried out following the same protocol.

To study the release behavior, the obtained ICG-loaded MMCNs were dispersed in 3 mL of buffer and 1 mL of the dispersion was transferred into a dialysis bag which molecular weight cut off is 14 000 Da. Then, the dialysis bag was placed in PBS solution in shaking table at 37 °C. At desired time intervals, 1 mL solution was collected and 1 mL fresh buffer was added. All samples were performed in triplicate and measured by UV–vis–NIR spectroscopy at 780 nm.

ROS Measurement: ROS was determined by the fluorescence intensity of the probe DPBF using a fluorescence spectrophotometer. DPBF can interact with ROS and quench DPBF fluorescence, which depends on the amount of ROS. DPBF was dissolved in 50% (v/v) acetonitrile-water solution and the fluorescence emission spectra of 5 µg mL^{-1} DPBF were collected. The maximum of the spectra were plotted at 455 nm against the amount of irradiation time to show the time-dependent yield of ROS.

Measurement of Photothermal Performance: To evaluate the photothermal behaviors, the nanoparticles were diluted to 50 µg mL^{-1}. Aliquots (100 µL) were deposited into wells of a 96-well cell culture plate. Wells were illuminated with a 785 nm continuous-wave NIR laser (fluence: 3 or 0.5 W cm^{-2}, spot size: 5 mm × 8 mm and exposure duration: 0–500 s). The temperature was measured by a thermocouple with an accuracy of 0.1 °C inserted into the dispersion. The photothermal effect of other nanomaterials was determined with a concentration of 50 µg mL^{-1} at the same conditions.

Cell Culture: A549 cells and 293T cells were purchased from Shanghai Xinran Biotech. Co., Ltd. (China) and cultured in RPMI-1640 medium and Dulbecco minimum essential medium individually supplemented with 10% (v/v) fetal bovine serum, 2 mm L-glutamine 100 U mL^{-1} of penicillin and 100 mg mL^{-1} of streptomycin at 37 °C and 5% CO$_2$.

Endocytosis Analysis: A549 cells and 293T cells were cultured in 6-well plates at a density of 1×10^5 cells mL^{-1} and incubated for 24 h to allow cell attachment. Then, the cells were incubated with the nanoparticles at indicated concentrations for 4 h. Next, the cells were collected after washing three times by PBS. In the end, the amount of nanoparticles endocytosis by cells was analyzed by flow cytometry.

Intracellular Localization of MMCNs: A549 cells were seeded in a confocal dish at a density of 1×10^5 cells mL^{-1} and incubated for 24 h to allow cell attachment. Then, the cells were incubated with the nanoparticles at indicated concentrations for 4 h. Next, the cells were washed by PBS for three times and stained with 200×10^{-9} M of Mitotracker (Invitrogen) or 250×10^{-9} M of Lysotracker (Molecular Probes) for 20 min and 5 µg mL^{-1} DAPI for another 10 min. After washing three times with PBS, the sample was subjected to laser scanning confocal microscopy. The subcellular colocalization was observed by CLSM and images of cells were collected under the same instrumental settings.

ICP-AES Quantification of Mitochondria-Targeting: A549 cells were seeded at a concentration of 1×10^6 cells mL^{-1} in a 175 cm^2 cell culture flask and incubated with MCN-Tf and MMCNs at a concentration of 50 µg mL^{-1} for 4 h. The medium was then removed and the cells were washed with PBS and trypsinized. After redispersed in PBS, the pellet was washed with ice cold PBS and collected via centrifugation at 800 g for 10 min. Mitochondria were isolated via differential centrifugation using a mitochondria isolation kit (Cat. NO: KGA828, KeyGEN BioTECH) following the producer's

instructions. Briefly, the collected pellets were redispersed in 1.5 mL of lysis buffer (delivered with the kit). The samples were then homogenized with a prechilled dounce homogenizer (7 mL, tight pestle A, 25 stokes) and centrifuged at 800 g for 5 min. The supernatant was transferred in a fresh tube containing the medium buffer C with a same volume and centrifuged at 15 000 g for 10 min at 4 °C. The obtained pellets were redispersed in Wash Buffer and centrifuged at 15 000 g for 10 min at 4 °C. The final pellets represented pure mitochondrial fractions. All samples were treated with HNO$_3$ to get clear solution and then the Fe concentrations were determined by ICP-AES (P-4010, HITACHI).

Intracellular ROS Level Measurement: A549 cells were seeded in 6-well plates and confocal dishes respectively at a density of 1×10^5 cells mL^{-1} and incubated for 24 h. Then cells were incubated with ICG-loaded MMCNs or ICG-loaded MMCNs and laser. 4 h later, 10×10^{-6} M DCFDA (a ROS probe, Ex: 488 nm, Em: 537 nm) was added into and cells were observed by a confocal microscope. Furthermore, the treated cells were also collected and observed by flow cytometry, and one group was further incubated 0.8×10^{-3} M NAC, (ROS inhibitor). CLSM images were collected under the same instrumental settings.

Live/Dead Cell Viability Assay: A549 cells were planked with a proper density and exposed to 50 µg mL^{-1} ICG-loaded MMCNs for 4 h. After laser irradiation at 785 nm (5 min, 0.5 W cm^{-2}), the cells were stained by calcein-AM and PI. Green fluorescence and red fluorescence indicated live cells and dead cells, respectively.

Apoptosis Assay: To investigate the form of cell death, 50 µg mL^{-1} ICG-loaded MMCNs in RPMI 1640 cell culture medium were added into a 6-well plate containing A549 cells. After 4 h, cells were exposed to laser irradiation at 785 nm (5 min, 0.5 W cm^{-2}), then the cells were stained by Annexin-V/PI and analyzed by flow cytometry.

MTT Assay: A549 cells were seeded in 96-well plates at a density of 5×10^3 viable cells per well and incubated for 24 h to allow cell attachment. Then the cells were incubated with the nanoparticles at indicated concentrations for 2 h. Afterward, the cells were exposed to a NIR laser (785 nm, 0.5 W cm^{-2}) for 5 min. After 24 h, the medium was replaced with fresh RPMI-l640 culture medium containing MTT (5 mg mL^{-1}), and the cells were incubated for an additional 4 h. Upon the removal of MTT solution, the purple formazan crystals generated by live cells were dissolved with dimethyl sulphoxide. The relative cell viability was determined by comparing the absorbance at 570 nm with control wells containing only cell culture medium.

Mouse Xenograft Model: To examine the treatment effect of ICG-loaded MMCNs, 4 weeks old male BALB/c nude mice were purchased from Shanghai BK Laboratory Animal Co., Ltd., China. Animal care and handing procedures were in agreement with the guidelines evaluated and approved by the ethics committee of Fudan University. Around 2×10^6 cells of A549 mixed with 200 µL PBS were subcutaneously injected in the right or left flank.

In Vivo Phototherapy: When the tumor volume attained to 100 mm^3, mice were randomly separated into six groups ($n = 6$ per group): PBS with laser treated (Group 1), ICG with laser treated (Group 2), ICG-loaded MMCNs with laser treated (Group 3), MMCNs with laser treated (Group 4), ICG-loaded MCNs-Tf with laser treated (Group 5), ICG-loaded MCNs-TPP with laser treated (Group 6). 100 µL of the above sample (0.5 mg mL^{-1}) was injected into mice by tail intravenous, respectively. After 6 h, the tumors were exposed to the

785 nm NIR laser at the power density of 0.5 W cm^{-2} for 5 min. The temperature of tumor site was recorded by an infrared camera. The size of tumor and mice weight were measured every other day. The tumor volume was calculated as $V = d^2 \times D/2$ (d: the shortest diameter of tumor, D: the longest diameter of tumor). At 14th d, the tumors and major organs (heart, liver, spleen, lung, and kidney) of mice were dissected and all the mice were euthanized. All tumors were weighed and parts of the organs and tumors were fixed in 4% formaldehyde solution for tissue slices.

In Vivo Fluorescence Imaging of MMCNs: To investigate the enrichment effect of ICG-loaded MMCNs in vivo, when tumor size reached around 500 mm^3, 100 μL (0.5 mg mL^{-1}) ICG-loaded MMCNs solution was injected into mice by tail intravenous. At proper time intervals, the fluorescence images were recorded by an optical and X-ray small animal imaging system (In Vivo Xtreme, Bruker).

Biodistribution of Nanoparticles in Mice: Four weeks old male mice were injected with ICG-loaded MMCNs intravenously. After 6 h, mice were treated with 785 nm laser at 0.5 W cm^{-2} power density. Then at different time intervals (10 min, 48 h, 14 d), mice were euthanized and major organs (heart, liver, spleen, lung, kidney) were dissected and weighed. All tissues were treated with HNO$_3$ to get clear solution and then the Fe concentrations were determined by ICP-AES.

Other Measurements: Optical absorption spectra were obtained by a Perkin-Elmer Lambda 750 spectrophotometer. The visualization of nanoparticles was performed on a Tecnai G2 TEM (FEI, USA). The size distribution of particles was measured by a Zetasizer Nano-ZS (Malvern) at 25 °C. N$_2$ adsorption–desorption isotherms were obtained on a Micromeritics Tristar 3000 pore analyzer at 77 K under continuous adsorption conditions. Brunauer–Emmett–Teller analysis was used to calculate the surface area. Thermal imaging was recorded by an infrared camera thermographic system (InfraTec, VarioCAMhr research, German). TGA of all samples was performed using a TGA assay (Pyris 1, Perkin-Elmer) with samples heated in alumina crucibles from 100 to 800 °C in a flowing air atmosphere with a scanning rate of 20 °C min^{-1}. Magnetic resonance images were acquired using a 7 T MRI instrument (BioSpec 70/30 USR, Bruker, German) equipped with a small animal coil at Cancer Research Institute of Fudan University.

Statistical Analysis: All data in this paper are expressed as mean result ± SD. Unpaired student's *t*-test was used for comparison between two testing groups and a probability (P) less than 0.05 was considered statistical significance.

Supporting Information

Supporting Information is available from the Wiley Online Library or from the author.

Acknowledgements

[1] a) A. Jemal, F. Bray, M. M. Center, J. Ferlay, E. Ward, D. Forman, *CA Cancer J. Clin.* **2011**, *61*, 69; b) D. Hanahan, R. A. Weinberg, *Cell* **2011**, *144*, 646.

[2] Q. Chen, H. Ke, Z. Dai, Z. Liu, *Biomaterials* **2015**, *73*, 214.

[3] a) Q. Tian, F. Jiang, R. Zou, Q. Liu, Z. Chen, M. Zhu, S. Yang, J. Wang, J. Wang, J. Hu, *ACS Nano* **2011**, *5*, 9761; b) A. P. Castano, P. Mroz, M. R. Hamblin, *Nat. Rev. Cancer* **2006**, *6*, 535.

[4] a) Z. Liu, L. Cheng, L. Zhang, Z. Yang, Z. Liu, J. Fang, *Biomaterials* **2014**, *35*, 4099; b) L. Cheng, C. Wang, L. Feng, K. Yang, Z. Liu, *Chem. Rev.* **2014**, *114*, 10869; c) E. S. Shibu, M. Hamada, N. Murase, V. Biju, *J. Photochem. Photobiol. C* **2013**, *15*, 53; d) J. Bhaumik, A. Mittal, A. Banerjee, Y. Chisti, U. Banerjee, *Nano Res.* **2015**, *8*, 1373.

[5] a) L. Guo, D. D. Yan, D. Yang, Y. Li, X. Wang, O. Zalewski, B. Yan, W. Lu, *ACS Nano* **2014**, *8*, 5670; b) C. S. S. R. Kumar, F. Mohammad, *Adv. Drug Delivery Rev.* **2011**, *63*, 789.

[6] P. Vijayaraghavan, C.-H. Liu, R. Vankayala, C.-S. Chiang, K. C. Hwang, *Adv. Mater.* **2014**, *26*, 6689.

[7] Y. Hu, Y. Yang, H. Wang, H. Du, *ACS Nano* **2015**, *9*, 8744.

[8] a) Z. Li, C. Wang, L. Cheng, H. Gong, S. Yin, Q. Gong, Y. Li, Z. Liu, *Biomaterials* **2013**, *34*, 9160; b) K. Lu, C. He, W. Lin, *J. Am. Chem. Soc.* **2014**, *136*, 16712; c) H. Wang, X. Yang, W. Shao, S. Chen, J. Xie, X. Zhang, J. Wang, Y. Xie, *J. Am. Chem. Soc.* **2015**, *137*, 11376.

[9] a) J. Lin, S. Wang, P. Huang, Z. Wang, S. Chen, G. Niu, W. Li, J. He, D. Cui, G. Lu, X. Chen, Z. Nie, *ACS Nano* **2013**, *7*, 5320; b) S. Wang, A. Riedinger, H. Li, C. Fu, H. Liu, L. Li, T. Liu, L. Tan, M. J. Barthel, G. Pugliese, F. De Donato, M. Scotto D'Abbusco, X. Meng, L. Manna, H. Meng, T. Pellegrino, *ACS Nano* **2015**, *9*, 1788.

[10] a) S. E. Weinberg, N. S. Chandel, *Nat. Chem. Biol.* **2015**, *11*, 9; b) H. Jin, A. Kanthasamy, A. Ghosh, V. Anantharam, B. Kalyanaraman, A. G. Kanthasamy, *Biochim. Biophys. Acta Mol. Basis Dis.* **2014**, *1842*, 1282.

[11] a) R. K. Pathak, N. Kolishetti, S. Dhar, *Wiley Interdiscip. Rev. Nanomed. Nanobiotechnol.* **2015**, *7*, 315; b) H. He, D.-W. Li, L.-Y. Yang, L. Fu, X.-J. Zhu, W.-K. Wong, F.-L. Jiang, Y. Liu, *Sci. Rep.* **2015**, *5*, 13543.

[12] H. S. Jung, J. Han, J.-H. Lee, J. H. Lee, J.-M. Choi, H.-S. Kweon, J. H. Han, J.-H. Kim, K. M. Byun, J. H. Jung, C. Kang, J. S. Kim, *J. Am. Chem. Soc.* **2015**, *137*, 3017.

[13] J. Liu, Y. Chen, G. Li, P. Zhang, C. Jin, L. Zeng, L. Ji, H. Chao, *Biomaterials* **2015**, *56*, 140.

[14] M. Chu, Y. Shao, J. Peng, X. Dai, H. Li, Q. Wu, D. Shi, *Biomaterials* **2013**, *34*, 4078.

[15] Y. Liu, K. Ai, J. Liu, M. Deng, Y. He, L. Lu, *Adv. Mater.* **2013**, *25*, 1353.

[16] a) N. K. Kildahl, *J. Chem. Educ.* **1995**, *72*, 423; b) Z. Sheng, D. Hu, M. Xue, M. He, P. Gong, L. Cai, *Nano-Micro Lett.* **2013**, *5*, 145; c) M. Zheng, C. Yue, Y. Ma, P. Gong, P. Zhao, C. Zheng, Z. Sheng, P. Zhang, Z. Wang, L. Cai, *ACS Nano* **2013**, *7*, 2056; d) C. Zheng, M. Zheng, P. Gong, D. Jia, P. Zhang, B. Shi, Z. Sheng, Y. Ma, L. Cai, *Biomaterials* **2012**, *33*, 5603; e) W. R. Chen, R. L. Adams, S. Heaton, D. T. Dickey, K. E. Bartels, R. E. Nordquist, *Cancer Lett.* **1995**, *88*, 15.

[17] M. Liong, J. Lu, M. Kovochich, T. Xia, S. G. Ruehm, A. E. Nel, F. Tamanoi, J. I. Zink, *ACS Nano* **2008**, *2*, 889.

[18] a) S. Marrache, S. Tundup, D. A. Harn, S. Dhar, *ACS Nano* **2013**, *7*, 7392; b) A. Sharma, G. M. Soliman, N. Al-Hajaj, R. Sharma, D. Maysinger, A. Kakkar, *Biomacromolecules* **2012**, *13*, 239; c) S. K. Bae, C. H. Heo, D. J. Choi, D. Sen, E.-H. Joe, B. R. Cho,

H. M. Kim, *J. Am. Chem. Soc.* **2013**, *135*, 9915; d) G. Masanta, C. S. Lim, H. J. Kim, J. H. Han, H. M. Kim, B. R. Cho, *J. Am. Chem. Soc.* **2011**, *133*, 5698.

[19] J. Liu, Z. Sun, Y. Deng, Y. Zou, C. Li, X. Guo, L. Xiong, Y. Gao, F. Li, D. Zhao, *Angew. Chem. Int. Ed.* **2009**, *48*, 5875.

[20] H. Lee, S. M. Dellatore, W. M. Miller, P. B. Messersmith, *Science* **2007**, *318*, 426.

[21] R. Zheng, S. Wang, Y. Tian, X. Jiang, D. Fu, S. Shen, W. Yang, *ACS Appl. Mater. Interfaces* **2015**, *7*, 15876.

[22] Y. Jiao, Y. Sun, X. Tang, Q. Ren, W. Yang, *Small* **2015**, *11*, 1962.

[23] S. Biswas, N. S. Dodwadkar, A. Piroyan, V. P. Torchilin, *Biomaterials* **2012**, *33*, 4773.

[24] E. C. Cho, Q. Zhang, Y. Xia, *Nat. Nanotechnol.* **2011**, *6*, 385.

[25] A.-K. Kirchherr, A. Briel, K. Mäder, *Mol. Pharmaceutics* **2009**, *6*, 480.

[26] S. Marrache, S. Dhar, *Proc. Natl. Acad. Sci. USA* **2012**, *109*, 16288.

[27] N. D. Sonawane, F. C. Szoka, A. S. Verkman, *J. Biol. Chem.* **2003**, *278*, 44826.

[28] S. Imstepf, V. Pierroz, R. Rubbiani, M. Felber, T. Fox, G. Gasser, R. Alberto, *Angew. Chem. Int. Ed.* **2016**, *55*, 2792.

[29] a) I. B. C. Matheson, J. Lee, B. S. Yamanashi, M. L. Wolbarsht, *J. Am. Chem. Soc.* **1974**, *96*, 3343; b) L. Wang, Q. Sun, X. Wang, T. Wen, J.-J. Yin, P. Wang, R. Bai, X.-Q. Zhang, L.-H. Zhang, A.-H. Lu, C. Chen, *J. Am. Chem. Soc.* **2015**, *137*, 1947.

[30] a) S. S. Lucky, N. Muhammad Idris, Z. Li, K. Huang, K. C. Soo, Y. Zhang, *ACS Nano* **2015**, *9*, 191; b) Y. Liu, Y. Liu, W. Bu, C. Cheng, C. Zuo, Q. Xiao, Y. Sun, D. Ni, C. Zhang, J. Liu, J. Shi, *Angew. Chem. Int. Ed.* **2015**, *54*, 8105; c) K. Deng, Z. Hou, X. Deng, P. Yang, C. Li, J. Lin, *Adv. Funct. Mater.* **2015**, *25*, 7280.

[31] a) N. Lee, T. Hyeon, *Chem. Soc. Rev.* **2012**, *41*, 2575; b) W. Cai, X. Chen, *Small* **2007**, *3*, 1840.

[32] D. Jaque, L. Martinez Maestro, B. del Rosal, P. Haro-Gonzalez, A. Benayas, J. L. Plaza, E. Martin Rodriguez, J. Garcia Sole, *Nanoscale* **2014**, *6*, 9494.

[33] a) A. Albanese, P. S. Tang, W. C. W. Chan, *Annu. Rev. Biomed. Eng.* **2012**, *14*, 1; b) W. H. De Jong, W. I. Hagens, P. Krystek, M. C. Burger, A. J. A. M. Sips, R. E. Geertsma, *Biomaterials* **2008**, *29*, 1912; c) S. M. Moghimi, A. C. Hunter, J. C. Murray, *FASEB J.* **2005**, *19*, 311.

[34] S. Tang, Q. Yin, Z. Zhang, W. Gu, L. Chen, H. Yu, Y. Huang, X. Chen, M. Xu, Y. Li, *Biomaterials* **2014**, *35*, 6047.

[35] R. Ahmed, A. Altieri, D. M. D'Souza, D. A. Leigh, K. M. Mullen, M. Papmeyer, A. M. Z. Slawin, J. K. Y. Wong, J. D. Woollins, *J. Am. Chem. Soc.* **2011**, *133*, 12304.